Journal of Colloid and Interface Science 718 (2026) 140532

Contents lists available at ScienceDirect

Journal of Colloid And Interface Science

journal homepage: www.elsevier.com/locate/jcis

Unravelling the mechanisms behind the stabilization of oil foams using soybean lecithin

Smaragda-Maria Argyri [a], Arnaud Saint-Jalmes [b], Carolina Ugarte-Pereyra [a], Romain Bordes [c], Sébastien Vincent-Bonnieu [d], Clémence Le Coeur [e,f], Bernard P. Binks [g], Emanuel Schneck [h,*], Anne-Laure Fameau [a,*]

[a] INRAE, University Lille, CNRS, Centrale Lille, UMET, 59000 Lille, France
[b] Université de Rennes, CNRS, IPR (Institut de Physique de Rennes), UMR 6251, F-35000 Rennes, France
[c] Department of Chemistry and Chemical Engineering, Chalmers University of Technology, 41296 Gothenburg, Sweden
[d] ESTEC, European Space Research and Technology Centre, Keplerlaan 1, Noordwijk 2201, AZ, Netherlands
[e] CNRS, ICMPE, UMR 7182, 2 Rue Henri Dunant, Université Paris Est Creteil, 94320 Thiais, France
[f] Laboratoire Léon Brillouin, Université Paris-Saclay, CEA-CNRS UMR 12 CEA Saclay, 91191 Gif sur Yvette, France
[g] Department of Chemistry, University of Hull, Hull. HU6 7RX. UK
[h] Institute for Condensed Matter Physics, TU Darmstadt, Hochschulstrasse 8, 64289, Darmstadt, Germany

GRAPHICAL ABSTRACT

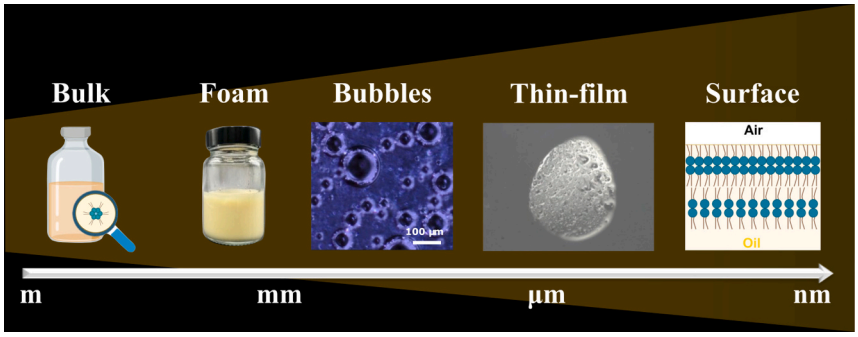

ARTICLE INFO

Keywords:
Non-aqueous
Oil foam
Interface
Self-assembly
Bubble
Surfactant

ABSTRACT

Oil foams are emerging as a promising, versatile system in food, cosmetic and pharmaceutical applications. Existing solutions depend on the addition of particles or surfactant crystallization; however, these approaches often require complex processing steps, introduce solid residues that may affect texture, and rely on kinetically trapped interfacial structures that limit reversibility under ambient conditions. Here, we examine the foamability and stability of food-grade, soybean lecithin in oil of different surface tension. We found that edible oil foams can be formed at room temperature only in long-chain triglyceride oils. By combining microscopy, X-ray techniques, and interfacial rheology, we show that the stabilization arises from the formation of inverse lipid bilayers at the air-oil surface, leading to increased surface elastic modulus and dense thin-films that protect the gas bubbles. We also discovered that different self-assembled structures are formed in different oils. These findings uncover a

* Corresponding authors.
E-mail addresses: emanuel.schneck@pkm.tu-darmstadt.de (E. Schneck), anne-laure.fameau@inrae.fr (A.-L. Fameau).

https://doi.org/10.1016/j.jcis.2026.140532
Received 26 February 2026; Received in revised form 1 April 2026; Accepted 13 April 2026
Available online 15 April 2026

molecular mechanism for non-aqueous foam stabilization under ambient conditions and establish design principles for surfactant-stabilized oil foams, without particle additives or crystallization.

1. Introduction

As global obesity levels are on the rise [1,2], the need for formulating food with an enhanced nutritional profile is in high demand from consumers and governmental agencies. Reducing the fat content by using fat replacers has been a well-established strategy in the food industry, towards providing nutritionally improved food options [3]. However, solid fats play key roles in shaping the sensory experience as they enhance flavor, mouthfeel, and aroma [4,5]. Oil foams offer a promising alternative to solid fats, by lowering the fat content while enhancing texture and sensory appeal [6–8]. Incorporating gas bubbles into oils has been patented as a method to partially replace fat in foods such as sponge cakes, biscuits, and laminated pastries [9–11].

In comparison to aqueous systems, formulating stable oil-based foams with surfactants is inherently challenging due to the low air-oil surface tension $\gamma_{a/o}$ of most oils (typically $\gamma_{a/o} \leq 35$ mN/m) and the lack of hydrophobic forces which drive surfactant adsorption at the air-water surface [12–16]. Historically, fluorocarbon-based surfactants were the most commonly used surfactant family for generating and stabilizing non-aqueous foams. Their effectiveness arises from the intrinsically low surface energy of fluorocarbon chains, allowing them to adsorb more strongly at the oil-air surface and reduce surface tension more effectively than hydrocarbon surfactants [17,18]. However, these surfactants are harmful and therefore unsuitable for food applications. In terms of food-grade solutions, two alternatives were recently identified for oils: crystalline surfactant particles [19,20] and hydroxyl-rich surfactants (*e.g.*, sorbitan esters [21], sucrose esters [22], and citric acid esters [23]). The hydrophilic groups of hydroxyl-rich surfactants can form hydrogen bonds with triglycerides in the oil phase forming complexes which are thought to lead to oil foam stabilization [21,22]. In contrast, crystalline particles are present at the bubble surfaces and in the continuous phase, leading to efficient oil foam stabilization [12,19,24,25]. However, both of these strategies are limited by the fact that oil foam formation only occurs above the melting point of the surfactant leading to temperature-dependent foam stability [19]. At present, no edible surfactants are known to produce oil foam at room temperature without heating or the use of solid particles, nor has a complete understanding of foamability and foam stability in such systems been established.

Herein, we demonstrate crystal-free oil foam stabilization at room temperature, using commercial, food-grade, fluid soybean lecithin (FSL) as a model hydrocarbon surfactant. We investigated the foamability and foam stability in three different oils: hexadecane as a model linear hydrocarbon oil, medium-chain triglyceride (MCT) oil, and sunflower oil (SFO) as a long-chain triglyceride oil. To unravel the stabilization mechanisms, we used a multi-scale approach encompassing the bulk phase, foam structure, bubbles, thin-films, and the air-oil surface. This study reveals for the first time the mechanisms of oil foam stabilization by hydrocarbon-based surfactants. These insights enhance the potential of using oil foams in food but also in the pharmaceutical and cosmetic industries.

2. Experimental section

2.1. Chemicals

FSL is a non-defatted lecithin (commercial grade, 42.7% phospholipids) was provided by Oleon Innovation (R&D), France (LECICO F 600 IPM, batch number 0.16–01–22-0007) and used as received. FSL is a group of phospholipids mainly consisting of phosphatidylcholine (PC), phosphatidylinositol (PI), phosphatidylethanolamine (PE) and phosphatidic acid (PA) purified from soybeans. According to the supplier, the phospholipids were 12.6% PC, 11.4% PI, 6.8% PE, 5.6% PA and 6.3% of other phospholipids. The fatty acid composition present in the hydrophobic tails of FSL was approximately 62% linoleic acid (C18:2), 15% palmitic acid (C16:0), 12% oleic acid (C18:1), 5% linolenic acid (C18:3) and 3% stearic acid (C18:0). The exact composition and quality specifications are presented in **Tables S1-S2**, respectively.

Sunflower oil (Cora, France), extra virgin olive oil (Cora, France), virgin sesame oil (Bio Cauvin, France) and linseed oil (Bio Cauvin, France) were purchased from a local store. The MCT oil was provided by BASF (Myritol 318®). Hexadecane was purchased from Sigma-Aldrich, France (99% purity). All chemicals were used and stored at room temperature.

2.2. Sample preparation

A series of FSL solutions (0.01–10.0 wt%) in hexadecane, MCT or sunflower oil was prepared by mixing the surfactant and oil phase at 700 rpm at 23 °C overnight. The solutions were stored at room temperature.

2.3. Oil foam preparation and characterization

The foamability of FSL in different oil phases was examined at concentrations ranging from 0.1 to 10.0 wt%. The foam was produced using an overhead stirrer type BS (Velp® Scientifica, Italy) with a milk frother extension connected to it (**Fig. S1, Supplementary Material**). 10 g of the samples were placed in glass vials (5.7 cm height and 3.4 cm diameter) and frothed for 3 min at room temperature. Photographs were collected before frothing, right after frothing and at regular intervals. From the photographs, the foam height was measured using the ImageJ software (version 1.47) and the overrun was calculated according to Eq. (1):

$$overrun\,(\%) = \frac{V_t - V_0}{V_0} \cdot 100 \quad (1)$$

Where V_0 is the initial volume of the mixture and V_t is the total volume after foaming.

After formation, the fresh foams were stored at room temperature. The stability of the foams was monitored over time by measuring the evolution of the foam volume, the volume of drained oil and the average bubble size with storage time.

2.4. Optical microscopy

Bulk FSL in oil solutions and the morphology of air bubbles within foams were analyzed using a Zeiss Axioscope 5 optical microscope with an Axiocam 208 camera (Zeiss, Germany), cross polarized light, and a temperature-controlled plate (Linkam, model LTS120) connected to a water circulation pump. The foam samples were transferred to the center of a glass slide by using a spatula and then gently covered with a coverslip. Images of individual bubbles were captured to observe structural characteristics including bubble size and distribution. The dimensions of about 100 bubbles from a minimum of 10 images were quantified using the ImageJ software (version 1.47).

2.5. Bulk characterization

The experimental details of differential scanning calorimetry, Karl-Fischer titration, and bulk viscosity are given in **Supplementary Notes S1.1 – S1.3**.

2.5.1. Small and wide-angle X-ray scattering

Small and wide-angle X-ray scattering measurements were performed at the French national synchrotron facility (Soleil, Saint-Aubin) on the SWING beamline. The experiments were performed at a 6038 mm sample-to-detector distance and wavelength λ of 1.02 Å to access a Q-range of 0.018 $Å^{-1}$ to 2.534 $Å^{-1}$, where Q is the magnitude of the scattering vector. The samples were loaded into quartz capillaries (optical path 1.5 mm, WJM-Glas/Müller, Germany) and placed on the sample changer and measured 10 times for 15 ms. The scattering from the empty cell and empty beam were removed from the raw data using the FoxTrot software, version 3.5. The data were fitted using the SASview software. More information on the models used for each sample can be found in **Supplementary Note S2.1**.

2.6. Surface characterization

2.6.1. Surface tension

The air-oil surface tension was measured using an automated surface tension plate reader, Kibron Delta-8 (Kibron, Finland) with DyneProbes. A volume of 50 µL of dispersion was placed on the 96-hole platform. The calibration was performed by filling the first row of the platform with milli-Q water at room temperature, in accordance with the user manual. Measurements of the samples were performed in triplicates after a waiting time of 10 min to ensure equilibrium at the air–oil surface. To ensure no oil remained on the DyneProbes, we rinsed them with ethanol, then immersed them in acetone, and sonicated them for 10 min. Lastly, the needles were dried with pressurized air.

2.6.2. Interfacial rheometry

The interfacial viscoelasticity at the air-oil surface was measured with an oscillatory rising bubble tensiometer (Tracker Teclis-IT Concept, France) through the oscillating pendant drop method [26]. We used a glass syringe (Hamilton™ 1000-series, USA) with a metallic needle connected to it (point style 3, 22 Ga, 0.718 mm external diameter). The oil droplet was pendant from the needle and was oscillated at a frequency of 0.1 Hz for a minimum of 10 min. The measured tension response was fitted with a linear viscoelastic model, and Fourier analysis was performed through the built-in software, calculating the amplitude and phase shift. From that the interfacial elastic and viscous moduli were extracted. The measurements were repeated a minimum of 3 times, and the standard deviation was calculated.

2.6.3. X-ray reflectometry

XRR measurements were performed using a D8 Advance reflectometer (Bruker AXS, Karlsruhe, Germany) as described in Ref. [27]. A sample volume was placed in a 60 × 40 ×2 mm Teflon trough (Kibron, Finland) and reflectivity curves were measured in the θ–2θ geometry where θ is the incident angle. The angular reflectivity scans were transformed into reflectivity curves as a function of the perpendicular scattering vector component, $Q_z = (4\pi/\lambda)\sin(\theta)$. Further experimental details are presented in the **Supplementary Note S1.4**. The details regarding the data analysis are given in **Supplementary Note S2.2**.

2.6.4. Grazing-incidence X-ray scattering

The experiments were carried out at the beamline P08 [28,29] at the storage ring PETRA III of the Deutsches Elektronen-Synchrotron (DESY, Hamburg, Germany). We used a modified Microtrough G4 (Kibron Inc., Finland) with dimensions 350 × 155 × 5 mm, and added 2 glass plates which reduced the required sample volume from 280 mL to 80 mL. The following descriptions are partially reproduced from references [30, 31]. The oil-filled Teflon trough was placed in a hermetically sealed helium-filled container with Kapton windows, and the temperature was kept at 20 °C with the help of a thermostat. The X-ray beam was monochromatized to a photon energy of 15 keV, corresponding to a wavelength of $\lambda = 0.826$ Å. The incident angle was $\alpha_i = 0.07°$, about 85% of the critical angle of total reflection $\alpha_c \approx 0.082°$ of the air-oil surface. Further experimental details are given in **Supplementary Notes S1.5–S1.7**. The data analysis is given in **Supplementary Note S2.3.**

2.6.5. Thin-film microscopy

The apparatus of this technique was adapted from Refs. [32, 33], where a freely suspended liquid film was created and held horizontally within a hole drilled through a solid support. The solid support is a porous glass frit filled with the foaming solution, thus mimicking the meniscus (Plateau borders) around a film in a real foam. Here, the diameter of the hole is 1.2 mm; this length thus corresponds to the diameter of a bubble face. Videos of the thin-films were recorded using a standard optical microscope from Olympus under reflected light. For each sample, a minimum of 10 thin-films were formed and examined. Further experimental details are given in **Supplementary Note 1.8**.

3. Results

3.1. Oil foam formation and stability for oil of different surface tension

We studied three model oils exhibiting different air-oil surface tensions with a fixed concentration of 5.0 wt% FSL (**Table S3, Supplementary Material**). We chose hexadecane as a low surface tension oil ($\gamma_{a/o} \approx 27.5$ mN/m), MCT (containing C_6-C_{10} chains) with an intermediate surface tension oil ($\gamma_{a/o} \approx 29.7$ mN/m), and SFO (containing mainly C_{18} chains) as a high surface tension oil ($\gamma_{a/o} \approx 32.5$ mN/m). The FSL was effectively dispersed in all oils after stirring overnight at room temperature, showing no crystal formation as observed by optical cross-polarized light (CPL) microscopy (**Fig. S2, Supplementary Material**). Subsequently, we tested foam formation by frothing at room temperature. Hexadecane showed no foam formation while MCT produced only a thin foam layer. On the contrary, SFO generated a high amount of foam (Fig. 1**.a-c**). Foam formation was also observed for other long-chain triglyceride oils of similar surface tension to SFO: linseed, sesame and olive oils (**Fig. S4, Supplementary Material**).

We varied the FSL concentration from 0.1 wt% to 10.0 wt% to determine the correlation between concentration and foam properties in SFO. No crystal formation was detected at high FSL concentration using CPL microscopy (**Fig. S3, Supplementary Material**). We then monitored the overrun (see Eq. (3)), foam volume, bubble size and bubble shape over time. At 0.1 wt%, no foam was observed, while at 0.5 wt% only a few bubbles were stabilized (Fig. 2**.a**). The overrun increased with FSL concentration from 54% ± 2% at 1.0 wt% to 142% ± 3% at 10.0 wt % (**Fig. S5, Supplementary Material**). Similar overruns were obtained regardless of the long-chain triglyceride oil used (**Table S4, Supplementary Material**). The CPL microscope images of the foams are shown in Fig. 2**.b,** where spherical bubbles with smooth surfaces were visible irrespective of FSL concentration. This indicates that these oil foams are stabilized by surfactant molecules, in contrast to surfactant-crystal stabilized bubbles where non-spherical bubbles are present [19]. There was a gradual decrease in bubble diameter with FSL concentration, as more surfactant molecules were available for bubble stabilization (**Fig. S6, Supplementary Material**).

Foam stability over time was monitored at room temperature for FSL foams in SFO ranging from 1.0 to 10.0 wt% (Fig. 3). Initially, all oil foams were relatively wet, with an air fraction below 0.6, resembling a bubbly oil phase rather than closely packed bubbles. During the first few minutes, oil drainage dominated, increasing the air fraction and transitioning into the “foam regime,” characterized by thin liquid films between the bubbles [34]. At 1.0 wt%, drainage was rapid: Foam volume declined sharply within 15 min, leaving only a thin layer after 3 h. Increasing FSL concentration reduced drainage significantly: At 10.0 wt %, minimal drainage occurred within 15 min, and substantial foam persisted after 3 h. The foam drained without coalescence during the first hours, then gradually reduced in volume after 24 h, remaining stable for 1–2 days. Similar stability trends were observed for other high surface tension vegetable oils. (**Fig. S7, Supplementary Material**).

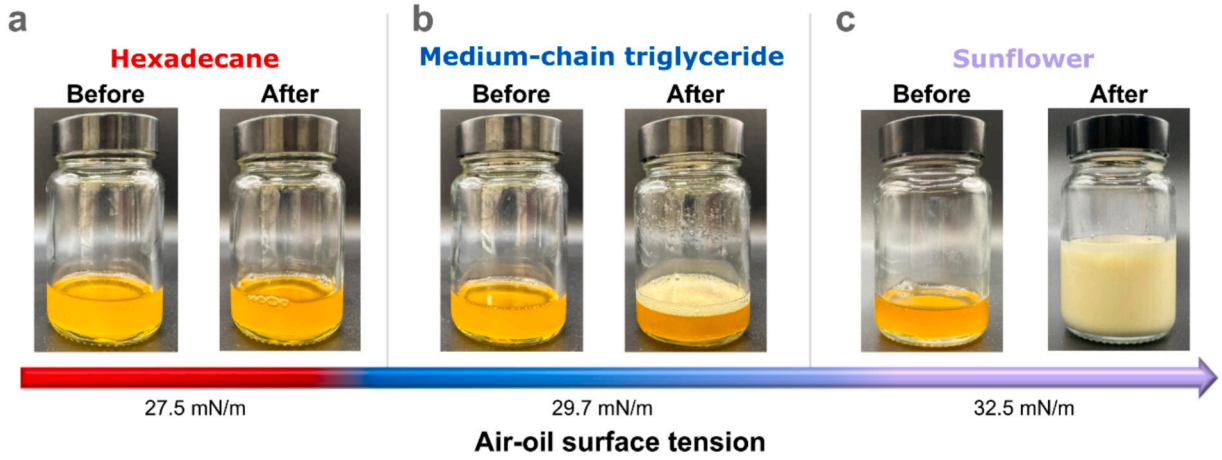

Fig. 1. Photographs showing the FSL samples before and after frothing for (a) hexadecane, (b) MCT oil, and (c) sunflower oil.

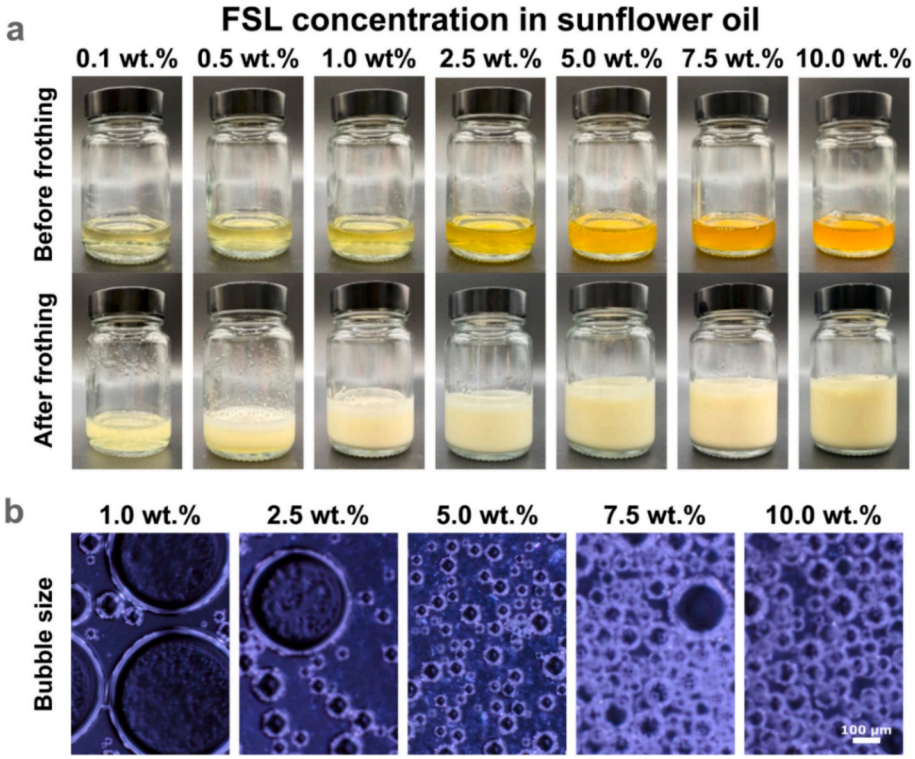

Fig. 2. (a) Photographs showing the samples before and immediately after frothing. (b) Optical cross-polarized light (CPL) microscopy images of oil foams right after frothing. Large, highly polydisperse, spherical bubbles were observed at 1.0 wt% with bubble diameters of around 121 ± 74 µm. By increasing the FSL concentration to 10.0 wt% the bubble diameter decreased to 70 ± 20 µm and the bubbles remained spherical in shape. All images share the same scale bar.

3.2. Fluid soybean lecithin behavior in bulk oil

To investigate the self-assembled structure of FSL in the bulk, we collected small angle X-ray scattering (SAXS) diffractograms at various FSL concentrations (Fig. 4). Already at low concentrations (0.05 wt%), we observed an increase in scattering intensity at low scattering vector magnitudes Q for each oil indicating the formation of self-assembled structures [35]. When dividing each scattering curve by the respective FSL concentration, we obtained the same scattering profile (**Fig. S8, Supplementary Material**), indicating that the same structures are maintained irrespective of FLS concentration. We fitted all the SAXS curves at 1 wt% with the sphere model, demonstrating the presence of reverse micelles of different radii: 2.6 nm in hexadecane, 1.8 nm in MCT, and 2.1 nm in SFO (**Fig. S9.a-b, Supplementary Material**). A slightly different morphology was observed for SFO with 7.0 wt% FSL, for which the curves were better fitted with the prolate ellipsoid model with a 2.1 nm and 1.6 nm polar and equatorial radii, respectively (**Fig. S9.c, Supplementary Material**). A structure factor $S(Q)$ was required to fit the characteristic inter-particle correlation features of the curve. This observation is in agreement with the literature reporting similar elongated reverse micelles of FSL in rapeseed oil [36]. Water was present inside the reverse micelles [37] since all FSL/oil samples contained water (less than 0.1 wt%), as determined from Karl-Fisher titration (**Table S5, Supplementary Material**). The water comes from FSL (0.5 wt% water), which can be attributed to the hygroscopic nature of phospholipids present, such as phosphatidylcholine (**Tables S1–S2, Supplementary Material**). Moreover, for SFO, we observed a weak diffraction peak at $Q = 0.125$ Å^{-1} (corresponding to a periodic length of

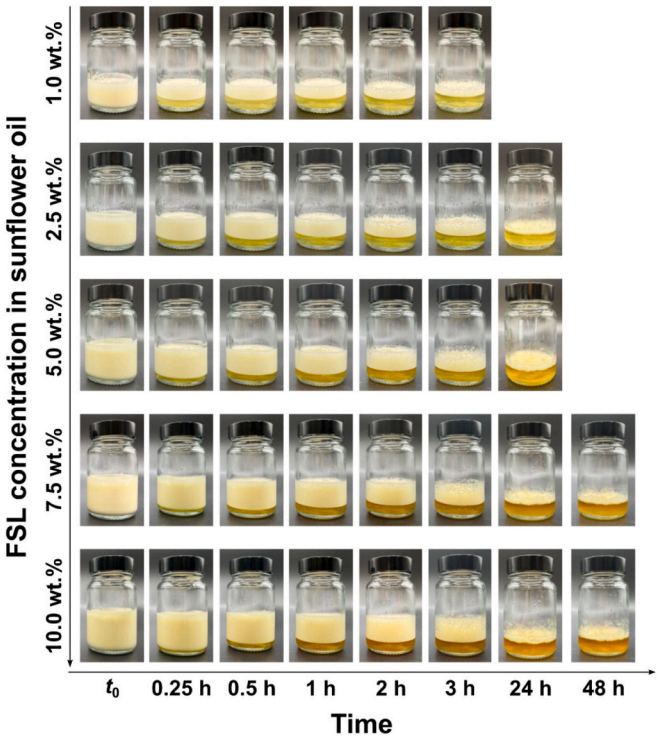

Fig. 3. Photographs showing the samples after frothing as a function of time and FSL concentration.

~5.0 nm), which seems to originate from lamellar structures formed by a small amount of undissolved FSL [36]. Here, we restrict our analysis to a qualitative identification of the lamellar phase. Indeed, it is important to notice that the fits from the sphere model do not fully reproduce the experimental curves, likely due to the intrinsic complexity of the system, as FSL is a mixture of phospholipids and sunflower oil a mixture of triglycerides. As a result, any quantitative decomposition of the scattering signal into micellar and lamellar contributions remains strongly model-dependent.

Wide-angle X-ray scattering (WAXS) (**Fig. S10, Supplementary Material**) was used to examine the small-scale structure in bulk. The broad peak observed at $Q = 1.38–1.39$ Å^{-1} for all three oils originates from a generic structural correlation of liquid hydrocarbon chains. The additional broad peaks observed at $Q = 0.28$ Å^{-1} for SFO and at $Q = 0.37$ Å^{-1} for MCT originate from the structural correlation between the polar groups of these two oils [38]. The addition of FSL introduces no new peaks, indicating the absence of small-scale crystallinity, consistent with CPL microscopy and DSC (**Fig. S2 and Fig. S11, Supplementary Material**)[17–19].

Next, we examined the bulk viscosity, which is another important parameter relevant to foam formation and stability (**Table S6, Supplementary Material**). In the case of FSL in SFO, we observed strong shear thinning behavior, in line with the presence of elongated micelles in bulk at high FSL concentrations. The addition of FSL in SFO led to a viscosity increase by approximately 160% at a shear rate of 1 s^{-1}. At low shear rates, a high bulk viscosity is known to enhance foam stability by slowing down liquid drainage, which explains the reduced oil drainage observed in foams with high FSL concentrations (Fig. 3). No shear thinning was observed for FLS in MCT and hexadecane (**Fig. S12, Supplementary Material**). In terms of foaming, it is known that low-viscosity media promote mixing and incorporation of air. Hexadecane and MCT exhibited lower viscosities at a shear rate of 100 s^{-1} (*i.e.*, rate similar to that during foam formation) compared to SFO (**Table S6, Supplementary Material**). Despite having lower viscosity than SFO, hexadecane and MCT showed little foaming, suggesting viscosity alone does not govern foamability.

3.3. Surface characterization of FSL at model air-oil surface

The above bulk characterization revealed the presence of self-assemblies and water in the bulk but could not explain why foam formation was observed only in SFO. Therefore, we continued by exploring the surface properties of FSL at model air-oil surfaces, starting with the air-oil surface tension $\gamma_{a/o}$ at different FSL concentrations. For hexadecane and MCT, $\gamma_{a/o}$ remained equal to the value of the pure oils across all FSL concentrations (**Fig. S13.a-b, Supplementary Material**). However, for SFO, a slight decrease in $\gamma_{a/o}$ from 32.7 mN/m to 31.5 mN/m was observed when the FSL concentration was above 0.5 wt% (**Fig. S13.c, Supplementary Material**). FSL lowered $\gamma_{a/o}$ only in long-chain triglyceride oils with the highest air–oil surface tension (**Fig. S13.d-f, Supplementary Material**). Interfacial dilatational rheology was used to assess the viscoelasticity of the surface layers. For FSL in hexadecane, the elastic modulus E' was extremely low (~0.3 mN/m), while a slightly higher elastic modulus was obtained in MCT (~7.8 mN/m). A very high interfacial elastic modulus was obtained for FSL in SFO (~61.7 mN/m), indicating a mechanically strong and cohesive layer adsorbed at the air-oil surface.

We then used X-ray reflectometry (XRR) to determine the structure of layers adsorbed at the air–oil surface, as this technique reveals the interfacial electron density profile $\rho_e(z)$, where z is the direction perpendicular to the surface. The XRR curves were analyzed on the basis of slab models (see **Supplementary Note S2**) that comprise stratified layers of lipid hydrocarbon chains (HC), lipid headgroups (HG) and water (W) with adjustable thicknesses d, and adjustable electron

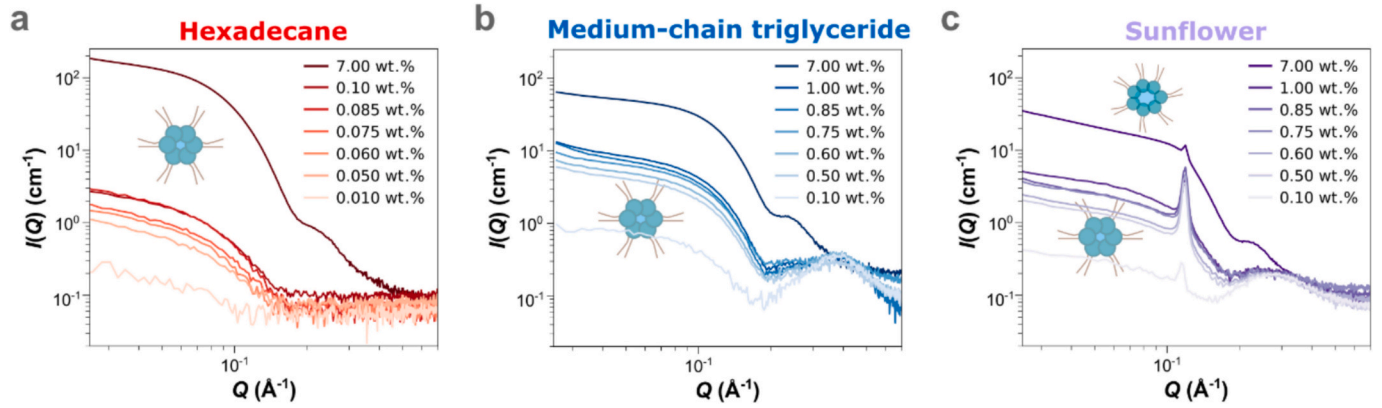

Fig. 4. SAXS curves of FSL dissolved at different concentrations in: (a) hexadecane, (b) MCT oil and (c) SFO. Reverse micelles are illustrated by schematics for all oil phases, while in the case of FSL in SFO elongated reverse micelles are illustrated at the top, in accordance with the fittings.

densities ρ_e. For all well-defined layers we obtained thicknesses of $d_{HC} = 1.6 \pm 0.2$ nm, $d_{HG} = 1.0 \pm 0.3$ nm and $d_W = 0.3 \pm 0.1$ nm, in agreement with the literature on single and interacting phospholipid layers [27,39–41].

The XRR curve for air-hexadecane containing FSL was best fitted with a model consisting of a single inverse bilayer (IBL) (Fig. 5**.a**). The outermost monolayer exhibited the lowest electron density, indicating low lateral molecular packing at the surface. In contrast, the inner layer showed a higher electron density, suggesting a more tightly packed and organized structure. This gradient in electron density reflects differences in molecular arrangement across the IBL, with the inner layer contributing more strongly to interfacial cohesion and stability. This structure of a fluid layer, loosely packed and lacking mechanical cohesion, is consistent with the extremely low elastic modulus. The XRR curve for air-MCT was fitted well using the same model of a single IBL (Fig. 5**.b**). Also in this case, the inner layer exhibits denser lipid packing than the outer one. The overall electron density at the surface is higher than that observed in hexadecane, indicating a more compact and structured lipid arrangement at the air-MCT interface, again in accordance with a moderate elastic modulus. The same single IBL model did not fit the XRR curve from the air-SFO surface (Fig. 5**.c, dashed black line**). Instead, a double IBL fitting model was required (Fig. 5**.c, red line**). This dense double IBL structure explains why the surface elastic modulus is much higher for FSL in SFO in comparison to the other oils. The exact thickness, density, and roughness parameters for each curve are reported in **Table S7–9, Supplementary Material**.

To determine the elemental composition at the air-oil surface, we performed synchrotron-based total-reflection X-ray fluorescence (TRXF) spectroscopy (**Notes S1**, **and Note S2.3**, **Supplementary Material**). In all oils, phosphorus was found to be enriched in the immediate vicinity of the surface, thus confirming the surface activity of FSL which carries a phosphorus atom in its headgroup. Specifically, the surface excess of phosphorus was 4.3 nm^{-2} for hexadecane, 5.4 nm^{-2} for MCT, and 6.5 nm^{-2} for SFO. When assuming a phosphorus density of 2 nm^{-2} in a phospholipid monolayer with a typical [42] area per lipid of 0.5 nm^2, then the obtained values roughly correspond to two monolayers (hexadecane), two and a half monolayers (MCT) and three monolayers (SFO). This is in line with the architecture revealed by XRR when accounting for the presence of some additional unstructured FSL near the surface of MCT and for the more loosely packed nature of the secondary IBL for SFO. Additionally, the spectra revealed an enrichment of monovalent and divalent cations near the surface [43], as seen for example from the increased intensity of the emission lines of K^+ and Ca^{2+} (Na^+ cannot be seen with TRXF). This observation suggests that the surface-adsorbed FSL layers are hydrated and loaded with counterions, compensating for the negatively charged lipid species present in FSL samples (**Fig. S14, Supplementary Material**).

Grazing-incidence small-angle and X-ray diffraction (GISAXS/GIXD) were employed to probe structural correlations in the interfacial region. Under total external reflection, the X-ray penetration depth is limited to ~10 nm, sampling only the near-surface layer. The GISAXS/GIXD patterns show all correlation peaks observed in SAXS/WAXS data from pure oils and FSL-containing samples (**Fig. S15–S16, Supplementary Material**). The corresponding peak positions agree within experimental uncertainty, and the GISAXS/GIXD peaks appear as Scherrer rings, indicating isotropic, undeformed structures. Thus, aside from the well-defined interfacial FSL layers revealed by XRR, the oil near the surface largely retains its bulk characteristics. It should be noted that our XRR-based observations of one or more IBL formed at the surface together with GISAXS and GIXD features that are consistent with SAXS can be

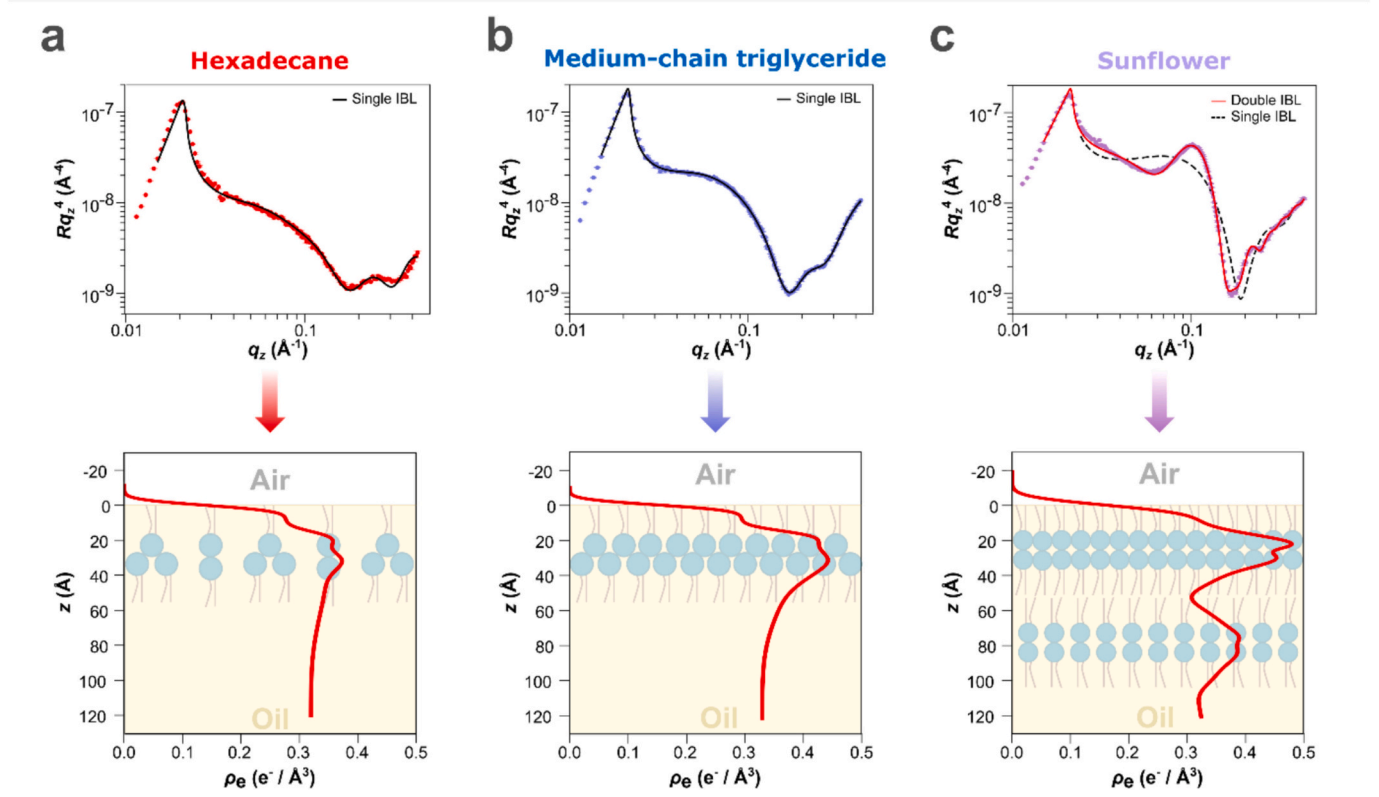

Fig. 5. (top row) X-ray reflectivity curves expressed as Porod-scaled reflectivity $R(q_z)*q_z^4$ in a double-logarithmic representation of (a) air-hexadecane, (b) air-MCT and (c) air-SFO surfaces. In the case of hexadecane and MCT, a single IBL fit (black line) describes the data well. In the case of SFO, the single IBL fit (black line) does not describe the data while a double IBL fit (red line) describes the data sufficiently. In all cases, the FSL concentration was 5.0 wt% (bottom row). Reconstructed electron density profiles ρ_e (z) with respect to the direction perpendicular to the surface z, together with illustrations of the associated interfacial arrangements of FSL. (For interpretation of the references to color in this figure legend, the reader is referred to the web version of this article.)

considered robust and do not rely on any knowledge or assumptions about the interaction between reverse micelles and interfacial layers. Quantitative modelling of the GISAXS data of surfactant-loaded air/oil interfaces, as was previously done in the framework of the distorted-wave Born approximation (DWBA) [44], for example for solid-supported lipid bilayers [45] and surface-adsorbed nanoparticles [46], might help elucidating the interaction between reverse micelles and interfacial layers in the future.

Furthermore, there are two important phenomena that are only observed with SFO (oil with the highest surface tension): (1) Lecithin forms more than one IBL at the air/oil surface, as evidenced by XRR, and (2) lecithin forms small amounts of lamellar structures in bulk oil in addition to reverse micelles, as evidenced by the Bragg peak in the SAXS curve. We propose that both phenomena may be attributed to the same mechanism based on the comparatively high surface tension of SFO. According to Antonov's rule[47], the interfacial tension $\gamma_{1,2}$ between two media can be approximated as the difference between their surface tensions in air, γ_1 and γ_2: $\gamma_{1,2} = |\gamma_2 - \gamma_1|$. Next, we assume that one medium is the oil, while the other is the FSL layer ensemble. The latter can be treated as a distinct medium because the amphiphilic nature of FSL renders it immiscible with oil. We note that the interface between the FSL medium and either air or oil will always be formed by the hydrophobic tails. This follows from the ILB architecture observed at the air/oil surface and is also consistent with free-energy considerations. Since the chemistry of the lecithin tails is essentially that of pure alkane oil, we may therefore approximate as $\gamma_{fsl/oil} \approx \gamma_{air/oil} - \gamma_{air/alkane}$. Based on these considerations, we conclude that a significant interfacial tension can exist between the FSL layers and the surrounding oil, and that this tension is substantially higher for SFO ($\gamma_{fsl/oil} \approx 5$ mN/m) than for the other two oil types investigated ($\gamma_{fsl/oil} < 1$ mN/m). With this notion in mind, it is straightforward to understand why individual IBLs tend to aggregate in SFO to form multilamellar structures: in doing so, the extent of the free-energetically unfavorable oil/FSL interface is minimized.

3.4. Oil foam stabilization mechanism: Thin-film characterization

To elucidate the mechanisms responsible for bubble stabilization, we examined the thickness and stability of thin-films (air-oil-air). For hexadecane, the films were highly unstable and ruptured within 10–20 s (**Supplementary Video 1**). The presence of multiple interference colors and visible flow patterns indicated a fluid and inhomogeneous film (Fig. 6.**a**). The film thickness decreased rapidly, exhibiting dynamic swirls associated with low viscosity, until reaching thicknesses of ~100–200 nm owing to the low surface coverage of FSL and the formation of only a single IBL. As a result, the films ruptured easily, correlating with the lack of foam formation. For MCT, the thin-film exhibited slightly greater stability over time compared to hexadecane, likely due to higher surface coverage by FSL (Fig. 6.**b**). Similarly, the films remained thin and fluid (**Supplementary Video 2**). However, for SFO, the film remained remarkably stable over time exhibiting a dense and inhomogeneous structure characterized by large, irregularly shaped domains (**Supplementary Video 3**) with an estimated thickness of 0.5–1 μm (above the color regime of interference). This can be attributed to the dynamic confinement of the dense packing of multiple IBLs at the air-oil surface and the presence of elongated reverse micelles in oil within the film, which cannot drain, getting jammed under confinement (Fig. 6.**c**). It is important to note that the thin film thickness was only determined qualitatively based on the observed colors and visual appearance of the thin films.

4. Conclusion

Here, we demonstrated for the first time that food-grade FSL, a hydrocarbon-based surfactant, can stabilize edible oil foams from long-chain triglyceride oils at room temperature. Contrary to previous works

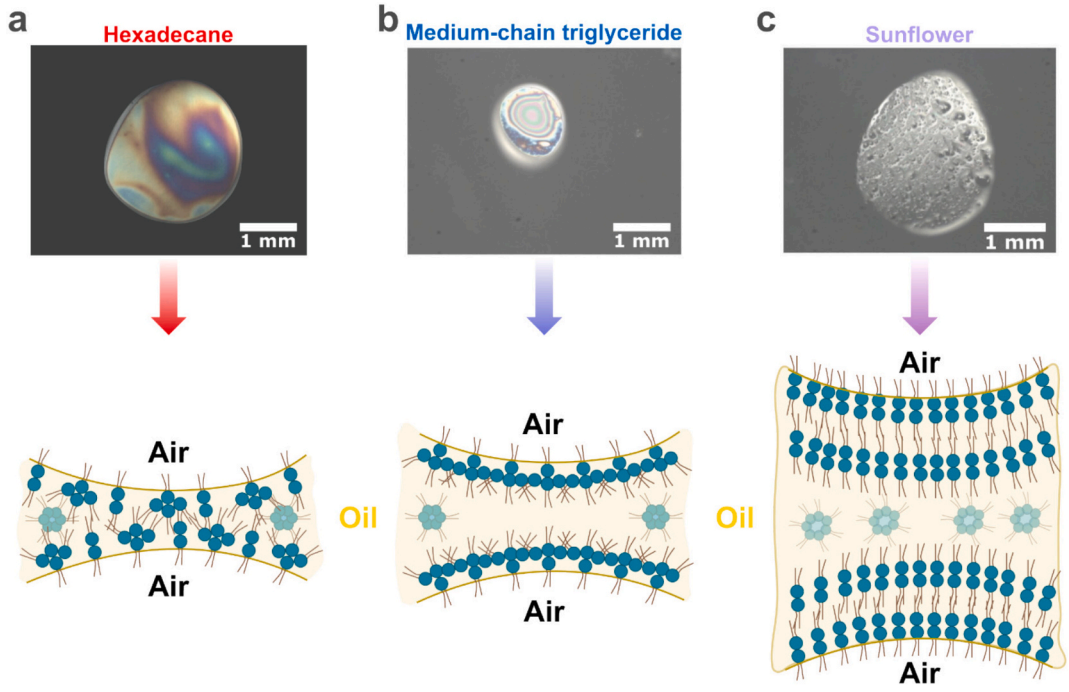

Fig. 6. (a) Thin-film microscopy image of 5 wt% FSL in hexadecane collected 10 s after formation. The film broke after 10–20 s which can be attributed to low surface coverage as shown in the schematic under it. (b) Thin-film microscope image of 5 wt% FSL in MCT collected 3.5 min after formation. The film broke after ~9.4 ± 0.5 min correlated to insufficient steric repulsion produced by a single IBL as shown in the schematic under it. (c) Thin-film microscope image of 5 wt% FSL dispersed in SFO collected 40 s after formation which remained unchanged for over 30 min. The thin-film was substantial in thickness and stable due to the presence of two IBLs as illustrated under it. A gel-like film forms at the surface and within the foam film, correlated to steric repulsion from overlapping layers of adsorbed surfactant molecules. These steric interactions hinder film rupture thereby enhancing foam stability.

[9–11,19,21,22], which rely on the use of crystalline surfactant particles to stabilize oil foams, we showed that such crystalline particles are not necessary.

SAXS revealed the presence of reverse micelles in all oils; however, no foam formed in the low surface tension oil (hexadecane), and only a few bubbles were stabilized in the intermediate one (MCT). On the contrary, the high surface tension oil (SFO) possessed elongated reverse micelles at high FSL concentrations, increasing bulk viscosity at low shear rates and enhancing foam stability by slowing down the drainage. The addition of FSL did not lead to any significant decrease in the surface tensions of hexadecane and or MCT, while a slight decrease was measured in SFO. Yet, X-ray reflectometry revealed that FSL forms inverse bilayers at the surface of all oils, albeit with oil-type-dependent densities and architectures (single *vs.* double IBL). For hexadecane and MCT, only a single, loosely packed IBL was present at the air-oil surface. This layer lacks the necessary elastic modulus and mechanical strength resulting in rapid film rupture and the inability to form foams. For MCT, the surface coverage was slightly higher explaining why a few bubbles could be stabilized. In SFO, the presence of two dense IBLs at the surface and elongated bulk micelles, lead to the formation of dense, stable thin-films between gas bubbles. Both bulk viscosity and bulk confinement, combined with a dense interfacial layer give rise to steric repulsion, which appears to prevent film drainage and thereby significantly enhance foam stability similar to fluorocarbon-based surfactant stabilization in non-aqueous foams [17,48]. This clarifies that reverse micelles are absent at the air–oil surface, disproving the "surface-active inverse micelle" hypothesis and showing that inverse bilayer structures drive surface activity and foam stabilization [48,49].

The differences between the oils clearly illustrate the importance of the surface properties and chemical structure of the oils on the self-assembly behavior of FSL at the air-oil surface. The influence of oil chemical structure on the self-assembly of surfactants at oil-water interfaces and its impact on emulsion stabilization remains an open and actively researched question [50–53]. Our findings highlight that similar fundamental questions arise in the case of the air-oil surface and oil foam stabilization. Specifically, the nature, structure and chain length of the oil critically affect the surface organization of hydrocarbon-based surfactants like FSL, ultimately determining whether stable oil foams can be formed or not [51–53]. While the detailed molecular mechanism governing the formation of double IBLs remains to be clarified, the present work provides the first structural evidence linking interfacial bilayer organization to oil foam stability and establishes a foundation for future studies aimed at systematically investigating the role of oil molecular structure.

Future work should focus on systematically investigating the role of individual phospholipid components (*e.g.*, phosphatidylcholine, phosphatidylethanolamine, *etc.*) and their specific contributions to foam formation and stability. This will require well-defined model systems based on pure triglycerides with controlled chain lengths and degrees of unsaturation, as well as tailored mixtures representing real vegetable oil systems. In addition, studying pure phospholipids will help disentangle their individual effects. Complementary molecular simulations on such simplified systems could provide valuable mechanistic insights, particularly regarding surfactant assembly at air–oil surface. Overall, this new understanding of hydrocarbon-based oil foams opens new possibilities for the design of innovative food, but also cosmetic and pharmaceutical products, while enabling better control over industrial processes involving oil-based foam systems.

Supplementary data to this article can be found online at https://doi.org/10.1016/j.jcis.2026.140532.

CRediT authorship contribution statement

Smaragda-Maria Argyri: Writing – review & editing, Writing – original draft, Software, Investigation, Formal analysis, Data curation, Conceptualization. **Arnaud Saint-Jalmes:** Writing – review & editing, Supervision, Methodology, Investigation, Formal analysis, Data curation, Conceptualization. **Carolina Ugarte-Pereyra:** Writing – review & editing, Investigation. **Romain Bordes:** Writing – review & editing, Supervision, Methodology, Funding acquisition, Conceptualization. **Sébastien Vincent-Bonnieu:** Writing – review & editing, Validation, Project administration. **Clémence Le Coeur:** Writing – review & editing, Validation, Investigation, Formal analysis. **Bernard P. Binks:** Writing – review & editing, Validation, Methodology. **Emanuel Schneck:** Writing – review & editing, Writing – original draft, Validation, Supervision, Resources, Methodology, Investigation, Formal analysis, Data curation, Conceptualization. **Anne-Laure Fameau:** Writing – review & editing, Writing – original draft, Validation, Supervision, Resources, Project administration, Methodology, Investigation, Funding acquisition, Formal analysis, Conceptualization.

Declaration of competing interest

The authors declare that they have no known competing financial interests or personal relationships that could have appeared to influence the work reported in this paper.

Acknowledgements

This work was supported by the European Space Agency (contract number: I-2024-03418) project Oil Foam, CNES and CPER BiHauts Eco de France project Profoam. We would like to thank Mariana Aguilera Gonzalez for experimental support with the foaming experiments. We also acknowledge the financial support from GDR2019 CNRS/INRAE "Solliciter La Matiére Molle" (SLAMM) and the Synchrotron Soleil (beamline SWING) within the framework of the block allocating group (BAG), proposal No. 20231446. We warmly acknowledge all support of the SWING beamline and specifically the experimental support that was provided by Bastien Rousseau and Dr. François Boue. We would also like to thank Dr. Sylvain Prevost for his support and scientific input on fitting the SAXS data.

We also thank Dr. Olaf Soltwedel for technical assistance with X-ray reflectivity measurements at the Technical University of Darmstadt and Prof. Dr. Regine von Klitzing for scientific discussions. We acknowledge DESY (Hamburg), a member of the Helmholtz Association HGF, for the provision of experimental facilities. Part of this research was conducted at PETRA III, DESY. We thank Dr. Chen Shen and Rene Kirchhof for assistance in using the P08 beamline and Milena Lippmann for assistance in the chemistry lab. Beamtime was allocated for proposal R-20240685 EC and we thank BMBF of Germany for funding the Eiger2 X 1 M detector through ErUM-Pro 05K19FK2 (Murphy, CAU Kiel).

The illustrations of the phospholipids and micelles were created on Biorender (available at: https://biorender.com). The Figures were formatted and finalized with InkScape version 1.2.2 (available at: https://inkscape.org). Created in BioRender. Fameau, A. (2026) https://BioRender.com/bzflgnt.

Data availability

Data will be made available on request.

References

[1] NCD Risk Factor Collaboration (NCD-RisC), Rising rural body-mass index is the main driver of the global obesity epidemic in adults, Nature 569 (2019) 260–264, https://doi.org/10.1038/s41586-019-1171-x.

[2] C. Ge, J. Xiong, R. Zhu, Z. Hong, Y. He, The global burden of high BMI among adolescents between 1990 and 2021, Commun. Med. 5 (2025) 1–13, https://doi.org/10.1038/s43856-025-00838-2.

[3] Y. Cao, R. Mezzenga, Design principles of food gels, Nat. Food 1 (2020) 106–118, https://doi.org/10.1038/s43016-019-0009-x.

[4] A.R. Patel, R.A. Nicholson, A.G. Marangoni, Applications of fat mimetics for the replacement of saturated and hydrogenated fat in food products, Curr. Opin. Food Sci. 33 (2020) 61–68, https://doi.org/10.1016/j.cofs.2019.12.008.

[5] E. Savchina, A.L. Grosso, P. Massoner, K. Morozova, M.M. Scampicchio, G. Ferrentino, From liquid to solid: exploring techniques, applications, and challenges of structured oils as fat replacements in food formulations, Compr. Rev. Food Sci. Food Saf. 24 (2025) 1–34, https://doi.org/10.1111/1541-4337.70163.

[6] E. Dickinson, Advances in food emulsions and foams: reflections on research in the neo-Pickering era, Curr. Opin. Food Sci. 33 (2020) 52–60, https://doi.org/10.1016/j.cofs.2019.12.009.

[7] A. Mohanan, K. Harrison, D.M.L. Cooper, M.T. Nickerson, S. Ghosh, Conversion of pulse protein foam-templated oleogels into oleofoams for improved baking application, Foods 11 (2022) 1–20, https://doi.org/10.3390/foods11182887.

[8] M. Grossi, M. Zhao, J. Rao, B. Chen, Oleofoams and whipped emulsions: formation, characterization, and future role in the food industry, Trends Food Sci. Technol. 153 (2024) 104752, https://doi.org/10.1016/j.tifs.2024.104752.

[9] C. Gehin-Delval, H. Chisholm, W. Chung, H. Deyber, M.J. Destribats, Z.D. Gunes, C. Pelloux, Method for forming a laminated pastry, US Patent App. 16/ 327, 912. https://patents.google.com/patent/US20190200625A1/en%0Ahttps://patentimages.storage.googleapis.com/a1/14/92/4f0d18851462cb/US20190200625A1.pdf, 2019.

[10] Z.G. Deniz, S. Olivier, C. Helen, D. Hélène, P. Cindy, B.P. Binks, Lipid Based Foam, US 2018 / 0070598 A1. https://patents.google.com/patent/US20180070598A1/en?oq=US+2018%2F0070598+A1, 2018.

[11] H. Chisholm, Z.D. Gunes, C. Gehin-Delval, A. Nouzille, E. Garvey, M.J. Destribats, S.N. Chandrasekaran, J. Vieira, J. German, B.P. Binks, Aerated confectionery material. https://patents.google.com/patent/US20180064127A1/en, 2016.

[12] R. Heymans, I. Tavernier, K. Dewettinck, P. Van der Meeren, Crystal stabilization of edible oil foams, Trends Food Sci. Technol. 69 (2017) 13–24, https://doi.org/10.1016/j.tifs.2017.08.015.

[13] A.L. Fameau, A. Saint-Jalmes, Non-aqueous foams: current understanding on the formation and stability mechanisms, Adv. Colloid Interf. Sci. 247 (2017) 454–464, https://doi.org/10.1016/j.cis.2017.02.007.

[14] D. Langevin, Aqueous foams: A field of investigation at the frontier between chemistry and physics, ChemPhysChem 9 (2008) 510–522, https://doi.org/10.1002/cphc.200700675.

[15] S.G.K. Calhoun, V. Chandran Suja, G.G. Fuller, Foaming and antifoaming in non-aqueous liquids, Curr. Opin. Colloid Interface Sci. 57 (2022) 101558, https://doi.org/10.1016/j.cocis.2021.101558.

[16] T. Arnaudova, Z. Mitrinova, N. Denkov, D. Growney, R. Brenda, S. Tcholakova, Foamability and foam stability of oily mixtures, Colloids Surf. A Physicochem. Eng. Asp. 653 (2022) 129987, https://doi.org/10.1016/j.colsurfa.2022.129987.

[17] V. Bergeron, J.E. Hanssen, F.N. Shoghl, Thin-film forces in hydrocarbon foam films and their application to gas- blocking foams in enhanced oil recovery, Colloids Surf. A Physicochem. Eng. Asp. 123–124 (1997) 609–622, https://doi.org/10.1016/S0927-7757(96)03808-3.

[18] S.G.K. Calhoun, V. Chandran Suja, G.G. Fuller, Foaming and antifoaming in non-aqueous liquids, Curr. Opin. Colloid Interface Sci. 57 (2022), https://doi.org/10.1016/j.cocis.2021.101558.

[19] A.L. Fameau, B.P. Binks, Aqueous and oil foams stabilized by surfactant crystals: new concepts and perspectives, Langmuir 37 (2021) 4411–4418, https://doi.org/10.1021/acs.langmuir.1c00410.

[20] K. Mishra, J. Bergfreund, P. Bertsch, P. Fischer, E.J. Windhab, Crystallization-induced network formation of tri- and monopalmitin at the middle-chain triglyceride oil/air interface, Langmuir 36 (2020) 7566–7572, https://doi.org/10.1021/acs.langmuir.0c01195.

[21] Y. Liu, B.P. Binks, Fabrication of stable oleofoams with sorbitan ester surfactants, Langmuir 38 (2022) 14779–14788, https://doi.org/10.1021/acs.langmuir.2c02413.

[22] Y. Liu, B.P. Binks, A novel strategy to fabricate stable oil foams with sucrose ester surfactant, J. Colloid Interface Sci. 594 (2021) 204–216, https://doi.org/10.1016/j.jcis.2021.03.021.

[23] C. Ugarte Pereyra, S.-M. Argyri, R. Bordes, S. Vincent-Bonnieu, J. Beaucé, B. P. Binks, C. Le Coeur, A.-L. Fameau, Design of oleofoams from citric acid esters of mono − / diglycerides, Food Res. Int. 220 (2025) 117119, https://doi.org/10.1016/j.foodres.2025.117119.

[24] B.P. Binks, B. Vishal, Particle-stabilized oil foams, Adv. Colloid Interf. Sci. 291 (2021) 102404, https://doi.org/10.1016/j.cis.2021.102404.

[25] B. Hashemi, E. Assadpour, F. Zhang, S.M. Jafari, Oleo-foams and emulsion-foams as lipid-based foam systems: A review of their formulation, characterization, and applications, Crit. Rev. Food Sci. Nutr. 65 (2025) 787–810, https://doi.org/10.1080/10408398.2023.2281622.

[26] J. Benjamins, A. Cagna, E.H. Lucassen-Reynders, Viscoelastic properties of triacylglycerol/water interfaces covered by proteins, Colloids Surf. A Physicochem. Eng. Asp. 114 (1996) 245–254, https://doi.org/10.1016/0927-7757(96)03533-9.

[27] J. Pusterla, E. Scoppola, C. Appel, T. Mukhina, C. Shen, G. Brezesinski, E. Schneck, Characterization of lipid bilayers adsorbed to functionalized air/water interfaces, Nanoscale 14 (2022) 15048–15059, https://doi.org/10.1039/d2nr03334h.

[28] O.H. Seeck, C. Deiter, K. Pflaum, F. Bertam, A. Beerlink, H. Franz, J. Horbach, H. Schulte-Schrepping, B.M. Murphy, M. Greve, O. Magnussen, The high-resolution diffraction beamline p08 at PETRA III, J. Synchrotron Radiat. 19 (2012) 30–38, https://doi.org/10.1107/S0909049511047236.

[29] C. Shen, R. Kirchhof, F. Bertram, A grazing incidence diffraction setup for langmuir trough experiments at the high-resolution diffraction beamline p08 at PETRA III, J. Phys. Conf. Ser. 2380 (2022) 012047, https://doi.org/10.1088/1742-6596/2380/1/012047.

[30] T. Mukhina, G. Brezesinski, C. Shen, E. Schneck, Phase behavior and miscibility in lipid monolayers containing glycolipids, J. Colloid Interface Sci. 615 (2022) 786–796, https://doi.org/10.1016/j.jcis.2022.01.146.

[31] L. Mortara, T. Mukhina, H. Chaimovich, G. Brezesinski, N.F.A. van der Vegt, E. Schneck, Anion competition at positively charged surfactant monolayers, Langmuir 40 (2024) 6949–6961, https://doi.org/10.1021/acs.langmuir.3c04003.

[32] V. Bergeron, C.J. Radke, Equilibrium measurements of oscillatory disjoining pressures in aqueous foam films, Langmuir 8 (1992) 3020–3026, https://doi.org/10.1021/la00048a028.

[33] V. Bergeron, Forces and structure in thin liquid soap films, J. Phys. Condens. Matter 11 (1999), https://doi.org/10.1088/0953-8984/11/19/201.

[34] R.J. Pugh, Foaming, foam films, antifoaming and defoaming, Adv. Colloid Interf. Sci. 64 (1996) 67–142, https://doi.org/10.1016/0001-8686(95)00280-4.

[35] P. Lindner, J. Oberdisse, Neutrons, X-Rays, and Light: Scattering Methods Applied to Soft Condensed Matter, Second, Elsevier, 2024.

[36] P.A. Penttila, S. Vierros, K. Utriainen, N. Carl, L. Rautkari, M. Sammalkorpi, M. Osterberg, Phospholipid-based reverse micelle structures in vegetable oil modified by water content, free fatty acid, and temperature, Langmuir 35 (2019) 8373–8382, https://doi.org/10.1021/acs.langmuir.9b01135.

[37] N.M. Correa, J.J. Silber, R.E. Riter, N.E. Levinger, Nonaqueous polar solvents in reverse micelle systems, Chem. Rev. 112 (2012) 4569–4602, https://doi.org/10.1021/cr200254q.

[38] O. Fadel, L. Girard, D.G. Rodrigues, P. Bauduin, X. Le Goff, A. Rossignol-Castera, A. L'Hermitte, O. Diat, Micellization in vegetable oils: A structural characterisation, Colloids Surf. B: Biointerfaces 154 (2017) 279–286, https://doi.org/10.1016/j.colsurfb.2017.03.025.

[39] C.A. Helm, H. Möhwald, K. Kjör, J. Als-Nielsen, Phospholipid monolayer density distribution perpendicular to the water surface. A synchrotron x-ray reflectivity study, Epl 4 (1987) 697–703, https://doi.org/10.1209/0295-5075/4/6/010.

[40] J. Majewski, T.L. Kuhl, K. Kjaer, M.C. Gerstenberg, J. Als-Nielsen, J. N. Israelachvili, G.S. Smith, X-ray synchrotron study of packing and protrusions of polymer - lipid monolayers at the air-water interference, J. Am. Chem. Soc. 120 (1998) 1469–1473, https://doi.org/10.1021/ja973024n.

[41] L. Bange, O. Soltwedel, D. Seibel, R. von Klitzing, Pressure–distance curves of identical and dissimilar lipid membrane surfaces in water, The Journal of Physical Chemistry B 129 (51) (2025) 13188–13196.

[42] A. Hermelink, G. Brezesinski, Do unsaturated phosphoinositides mix with ordered phosphadidylcholine model membranes? J. Lipid Res. 49 (2008) 1918–1925, https://doi.org/10.1194/jlr.M700527-JLR200.

[43] L.G. Parratt, Surface studies of solids by total reflection of x-rays, Phys. Rev. 95 (1954) 359–369, https://doi.org/10.1103/PhysRev.95.359.

[44] M. Rauscher, T. Salditt, H. Spohn, Small-angle x-ray scattering under grazing incidence: the cross section in the distorted-wave born approximation, Phys. Rev. B 52 (1995) 52 16855. Doi: https://doi.org/10.1103/PhysRevB.52.16855.

[45] J. Daillant, E. Bellet-Amalric, A. Braslau, T. Charitat, G. Fragneto, F. Graner, S. Mora, F. Rieutord, B. Stidder, Structure and fluctuations of a single floating lipid bilayer, Proc. Natl. Acad. Sci. USA 102 (2005) 11639–11644, https://doi.org/10.1073/pnas.0504588102.

[46] L. Wu, X. Wang, G. Wang, G. Chen, In situ x-ray scattering observation of two-dimensional interfacial colloidal crystallization, Nat. Commun. 9 (2018), https://doi.org/10.1038/s41467-018-03767-y.

[47] L. Makkonen, K. Juha, Another look at the interfacial interaction parameter, Journal of colloid and interface science 529 (2018) 243–246. https://doi.org/10.1016/j.jcis.2018.06.015.

[48] S.E. Friberg, A. Al Bawab, A.A. Abdoh, Surface active inverse micelles, Colloid Polym. Sci. 285 (2007) 1625–1630, https://doi.org/10.1007/s00396-007-1734-5.

[49] S.E. Friberg, Applications of amphiphilic association structures, Adv. Colloid Interf. Sci. 32 (1990) 167–182.

[50] J. Bergfreund, S. Siegenthaler, V. Lutz-Bueno, P. Bertsch, P. Fischer, Surfactant adsorption to different fluid interfaces, Langmuir 37 (2021) 6722–6727, https://doi.org/10.1021/acs.langmuir.1c00668.

[51] A. Rahman, J. Eastoe, The effects of surfactant and oil chemical structures on self-assembly in apolar media, Soft Matter 18 (2022) 9133–9152, https://doi.org/10.1039/d2sm00827k.

[52] S. Hosseinpour, V. Götz, W. Peukert, Effect of surfactants on the molecular structure of the buried oil/water interface, Angew. Chem. Int. Ed. 60 (2021) 25143–25150, https://doi.org/10.1002/anie.202110091.

[53] P.G. De Gennes, C. Taupin, Microemulsions and the flexibility of oil/water interfaces, J. Phys. Chem. 86 (1982) 2294–2304, https://doi.org/10.1021/j100210a011.